Research Square

Preprints are preliminary reports that have not undergone peer review.
They should not be considered conclusive, used to inform clinical practice,
or referenced by the media as validated information.

A topology-dependent IRE1α signaling axis generates a cryptic XBP1 isoform present in human cancers

Maxwell Wilson

mzw@ucsb.edu

University of California Santa Barbara https://orcid.org/0000-0003-0768-7004

Jose Rodrigues Reyes

University of California, Santa Barbara https://orcid.org/0000-0001-9790-3502

Collin Vergel De Dios

University of California, Santa Barbara

Debalina Datta

University of California Santa Barbara

Taivan Batjargal

University of California Santa Barbara https://orcid.org/0000-0001-7882-4382

Surenna Pecchia

University of California, Santa Barbara

Feroz Papa

UCSF https://orcid.org/0000-0002-3684-9108

Article

Keywords:

Posted Date: June 4th, 2026

DOI: https://doi.org/10.21203/rs.3.rs-9695931/v1

License: This work is licensed under a Creative Commons Attribution 4.0 International License.
Read Full License

Additional Declarations: Yes there is potential Competing Interest. Maxwell Wilson is CTO and Co-founder of Integrated Biosciences

A topology-dependent IRE1α signaling axis generates a cryptic XBP1 isoform present in human cancers

Jose Roberto Rodrigues Reyes[1], Collin Vergel De Dios[2], Debalina Datta[3], Taivan Batjargal[4], Surenna Pecchia[2], Feroz R. Papa[3], Maxwell Z. Wilson[1,2]*

Affiliations

[1]Interdisciplinary Program in Quantitative Biosciences, University of California, Santa Barbara, Santa Barbara, CA, USA. [2]Department of Molecular, Cellular, and Developmental Biology, University of California Santa Barbara, Santa Barbara, CA, USA. [3]Neuroscience Research Institute, University of California Santa Barbara, Santa Barbara, CA, USA. [4]Department of Medicine, University of California, San Francisco, San Francisco, CA, USA.

*Corresponding author: Maxwell Z. Wilson. e-mail: mzw@ucsb.edu

Abstract:

IRE1α, the most conserved unfolded protein response sensor, is displaced from the ER during caspase-mediated cleavage, viral infection, and chronic stress, but the signaling consequences are unknown. Using optogenetic IRE1α constructs targeted to either the ER or the cytoplasm, we show that subcellular topology determines oligomerization dynamics, transcriptional output, and cell fate. ER-tethered IRE1α forms small, persistent clusters that efficiently splice XBP1 and engage RIDD. Cytoplasmic IRE1α coalesces into hyperclusters that drive cytoskeletal transcript decay and cell-cycle arrest without apoptosis, despite elevated phosphorylation. The kinase-pocket antagonist PAIR2 rescues proliferation while preserving RIDD, establishing that these outputs are pharmacologically separable. Cytoplasmic activation also generates XBP1-es, an exon 4-skipped isoform that retains UPR transcription factor activity but fails to induce ISR genes including ATF4 and CHOP, and is detectable in 10.9% of TCGA tumors, with highest prevalence in acute myeloid leukemia (60%) and breast cancer (27%).

Introduction:

The functional output of a signaling enzyme depends not only on its activation state but where in the cell it acts. This is well established for kinases[1–4] and second-messenger systems[5,6], where topological compartmentalization creates signaling specificity that cannot be achieved by activity alone. By contrast, whether subcellular topology directly governs the outputs of stress-sensing enzymes remains largely unexplored.

Inositol-Requiring Enzyme 1α (IRE1α) is the most evolutionarily conserved sensor of the Unfolded Protein Response (UPR) and the only human kinase-endoribonuclease to respond to the protein-folding status of the ER lumen[7–9]. Upon sensing misfolded proteins, ER-anchored IRE1α oligomerizes, trans-autophosphorylates, and activates its RNase domain to perform two molecularly distinct functions: frameshift splicing of XBP1-u (X-box binding protein 1 unspliced) mRNA to produce the transcript XBP1-s (XBP1-spliced), and Regulated IRE1α Dependent Decay (RIDD), the cleavage of an ER-localized subset of RNAs bearing endomotifs similar to the XBP1 splice site[7–9]. Together, these outputs can drive either adaptive or maladaptive cell fates, and the ratio between them is thought to be determined primarily by IRE1α's oligomeric state, with low-order assemblies favoring selective XBP1 splicing and high-order hyperclusters promoting broad mRNA decay and adverse outcomes[10–13]. A critical but

underappreciated feature of this model is that both substrate pools (e.g. XBP1u mRNA and RIDD targets) are themselves localized to the ER membrane, suggesting that substrate proximity to the ER is a prerequisite for efficient IRE1α RNase output[12,14]. By extension, displacement of IRE1α from the ER should fundamentally alter the substrates it encounters and consequently, the signaling program it engages.

Multiple disease-relevant contexts can displace IRE1α from the ER membrane. Caspase-mediated cleavage during apoptotic commitment releases the cytoplasmic kinase-RNase domain into the cytosol, an event observed in stressed multiple myeloma cells that has been linked to pro-survival signaling[15]. During Zika virus infection, both IRE1α and XBP1 translocate to the cytoplasmic viral replication complexes[16]. And earlier work on chimp cells documented nuclear accumulation of IRE1α fragments during ER stress[17]. In each case, IRE1α is re-localized to a topology where its canonical substrates are not. Whether this topological displacement constitutes a functionally distinct signaling state, or is merely a passive consequence of cellular damage, has not been directly tested (Fig. 1A).

Addressing these questions has been technically challenging because conventional ER stress inducers activate all three UPR branches simultaneously, making it difficult to isolate the contributions of IRE1α localization from stress level, cellular damage, activation kinetics, or parallel PERK and ATF6 signaling. Common inducers such as thapsigargin, which blocks SERCA pumps and tunicamycin, which inhibits *N*-linked protein glycosylation, create a complex response in which protein misfolding in the ER triggers translational suppression, and parallel ISR branch making causal attribution to any single sensor or signaling state impossible[18]. While genetic approaches that anchor or delete the transmembrane domain (TM) would remove the oligomerization-inducing luminal domain, killing protein activity. Additionally, existing chemogenetic approaches have been limited to inducing IRE1α dimerization, falling short of driving higher-order oligomerization[19]. Therefore, to address the question of topology-dependent signaling, what is required is a tool that both activates IRE1α oligomerization directly, in a topologically defined manner, and without physically damaging cells to induce stress.

Optogenetic tools that reversibly induce oligomerization circumvent this problem entirely. By fusing CRY2olig, a photosensitive domain that undergoes rapid and reversible homo-oligomerization upon blue light illumination, to the cytosolic domain of IRE1α, it is possible to activate the kinase-RNase signaling cascade without any upstream stress[20]. The approach was recently exploited to demonstrate that optogenetic activation faithfully recapitulates canonical UPR outputs, establishing opto-IRE1α as a validated platform for precise causal interrogation of UPR biology[10]. Here we leverage the property that CRY2oligs clustering mechanism is independent of the membrane topology of its fusion partner, operating equivalently whether IRE1α is anchored in the ER or freely diffusing in the cytoplasm. This property makes it possible to hold enzymatic activity, stress levels, and stress dynamics constant while varying only subcellular localization, thereby causally dissecting the role of IRE1α's relocalization, observed in disease.

Here, we use two complementary chemical biology approaches to dissect the role of IRE1α localization on signaling. Using optogenetic IRE1α constructs targeted to either the ER membrane or the cytoplasm, we find that topology alone is sufficient to fundamentally rewire

signaling output. ER-tethered IRE1α generates small, persistent oligomers that selectively target ER-proximal transcripts, while cytoplasmic IRE1α rapidly coalesces into hyperclusters that drive widespread RNA decay, spliceosome engagement, and cell cycle arrest without apoptosis. To dissect the downstream outputs that specifically require cytoplasmic cluster formation, we employ PAIR2 (Partial Antagonist of IRE1α RNase), an ATP-competitive antagonist that binds the IRE1α kinase pocket and preserves adaptive RNase activity while blocking terminal outputs[21]. We demonstrate that XBP1-s and RIDD activity are insufficient to drive growth arrest, implicating a kinase-dependent signaling axis as a key mediator of the arrest phenotype. Finally, we find that cytoplasmic IRE1α activation generates XBP1-es, a previously described XBP1 splice isoform lacking exon 4 that functionally decouples IRE1α signaling from the integrated stress response and is detectable in a significant fraction of The Cancer Genome Atlas (TCGA) tumors. Together, these findings establish topology as a primary spatial determinant of IRE1α signaling, expanding the canonical oligomerization model to incorporate where, not just how much, IRE1α clusters as a key variable in cell fate decisions.

Results:

Fig. 1: IRE1α hyperclusters exhibit unconstrained diffusion consistent with ER membrane release.

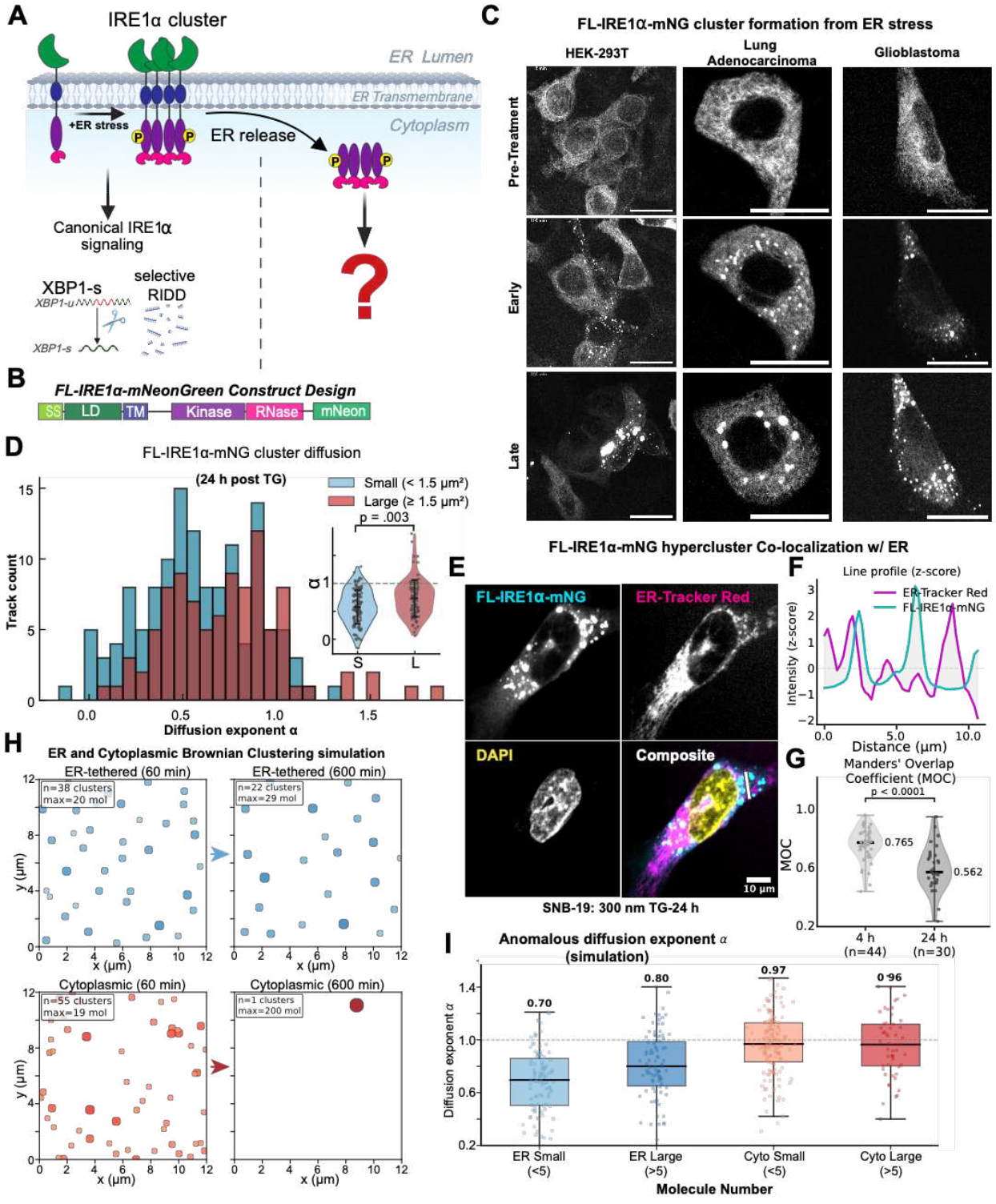


Figure 1: ***(A)*** *Schematic illustrating the hypothesis that prolonged ER stress displaces IRE1α from the ER membrane, enabling free three-dimensional diffusion and access to non-canonical cytoplasmic substrates.* ***(B)*** *Construct design for full-length IRE1α C-terminally tagged with mNeonGreen (FL-IRE1α-mNG) used to track endogenous oligomerization dynamics.* ***(C)*** *Representative confocal images of FL-IRE1α-mNG clusters in HEK293T, EKVX, and SNB-19 cells at early (4 h) and late (24 h) time points following treatment with 300 nM thapsigargin (TG). Scale bars, 10 μm.* ***(D)*** *Anomalous diffusion exponent (α) calculated from mean squared displacement (MSD) analysis of individual FL-IRE1α-mNG clusters in SNB-19 cells at 24 h post-TG, binned by cluster area. Small clusters (≤ 1.5 μm²) exhibit subdiffusive motion (α < 1) consistent with ER membrane confinement; large clusters (> 1.5 μm²) approach α ≈ 1.0, consistent with free Brownian diffusion in three dimensions. Each point represents a single cluster track; violin plots show median ± IQR. (p =0.003, two-tailed T-test, rank-biserial r =0.244)* ***(E)*** *Representative confocal image of a SNB-19 cell expressing FL-IRE1α-mNG and stained with ER-Tracker Red at 24 h post-TG, illustrating spatial separation of hyperclusters from the ER. Scale bar, 10 μm.* ***(F)*** *Z-scored line intensity profile along the ROI indicated in E, showing reduced co-localization between IRE1α hyperclusters and ER-Tracker Red signal at 24 h.* ***(G)*** *Manders' Overlap Coefficient (MOC) between FL-IRE1α-mNG and ER-Tracker Red from the segmented cytoplasm of SNB-19 cells at 4 h (n = 44 cells) and 24 h (n = 30 cells) post-TG. p < 0.0001 (two-sided Mann–Whitney U test, Hedges' g = -0.604).* ***(H)*** *Snapshots from a stochastic Brownian clustering simulation at 60 min and 600 min, comparing ER-tethered IRE1α (2D, corral-confined diffusion) with cytoplasmic IRE1α (3D free diffusion). Simulation parameters were drawn entirely from published literature (see Methods).* ***(I)*** *Anomalous diffusion exponent (α) computed from simulated cluster trajectories at 240 min for ER-tethered versus cytoplasmic conditions. Simulated α values recapitulate the experimental distribution in* ***D****, with ER-tethered clusters showing α < 1 and cytoplasmic clusters showing α ≈ 1.0. All simulation parameters are listed in Methods Table 1.*

IRE1α hyperclusters formed under chronic stress exhibit unconstrained diffusion consistent with release from the ER

To characterize IRE1α oligomerization dynamics under ER stress, we stably expressed full-length IRE1α tagged with mNeonGreen at the C-terminus (FL-IRE1α-mNG)[22] and tracked cluster formation in four cell lines (HEK293T, U2OS, lung adenocarcinoma (EKVX), and glioblastoma (SNB-19)) treated with 300 nM thapsigargin (Fig. 1B-C; Fig. S1A). All four lines formed IRE1α clusters that grew over time, though with cell-type differences. HEK293T, EKVX, and SNB-19 cells all formed clusters in response to stress that persisted and continued to enlarge (Supplementary Video 1). U2OS clusters initially grew but later dissolved (consistent with prior observations[22]) (Supplementary Video 2). We acquired high-temporal-resolution time-lapse images of FL-IRE1α-mNG clusters in SNB-19 cells, and calculated Mean Squared Displacement (MSD), Diffusion Exponent (D), and Anomalous Diffusion exponent (α) (Fig. S1F). We then binned clusters based on area making clusters >1.5 μm^2 to be called large clusters (Fig. S1B-C). Consistent with previous reports, D was unaffected by cluster size (Fig. S1D-E). In contrast, α revealed significantly less constrained diffusion for larger clusters (Fig. 1D). Because IRE1α is an ER transmembrane protein, we expected clusters to exhibit constrained diffusion regardless of size. Additional image analysis of FL-IRE1α-mNG stained with ER-Tracker Red revealed that their colocalization decreased during prolonged ER stress, as more hyperclusters formed (Fig. 1E-G). Together, these results indicate that during prolonged ER stress, IRE1α hyperclusters undergo a quantitative change in diffusion behavior, consistent with release from the ER membrane.

SEC61β is a general ER membrane protein routinely used as a reporter for ER localization. Prior quantitative imaging showed that although IRE1α oligomers maintain partial three-dimensional overlap with SEC61β signal, large clusters frequently contain interior regions from which SEC61β is excluded, suggesting that portions of these oligomers may no longer reside within a

contiguous ER membrane[22]. A plausible molecular basis for this displacement is the discovery that during prolonged ER stress, caspases cleave IRE1α between the luminal sensor and transmembrane domains (D507 and D512), liberating the cytosolic kinase-RNase fragment from the ER while the luminal-transmembrane fragment remains membrane-embedded[15]. This cleavage has been shown to abolish protective RNase activity and redirect cells toward apoptosis, but whether the released cytosolic domain can re-oligomerize and engage alternative substrates remains unexamined. We therefore asked whether the diffusive behavior of large IRE1α hyperclusters is consistent with partial or complete release from the ER.

To test whether dimensionality alone could explain this, we developed a stochastic Brownian clustering simulation comparing two limiting cases: ER-tethered IRE1α diffusing on a two-dimensional membrane partitioned into corrals mimicking the tubular ER network, and cytoplasmic IRE1α undergoing free three-dimensional Brownian motion (see Methods for full parameterization) (Fig. 1H-I, Supplementary Video 3). The two conditions share identical interaction rules and differ only in their diffusive transport; all parameters were drawn from published literature rather than fit to our data.

MSD analysis of simulated trajectories reproduced the experimental observation (Fig. 1D). In the 2D, ER-tethered clusters we observed $\alpha < 1$ across all sizes, while cytoplasmic clusters maintained $\alpha \approx 1.0$ (Fig. 1I). An α approaching 1.0 indicates Brownian motion unimpeded by membrane confinement or corral boundaries, the behavior expected of a freely diffusing cytoplasmic particle. The α values measured for large IRE1α clusters under prolonged ER stress exceeded the range predicted by the 2D ER-tethered simulation and fell within the range of the 3D cytoplasmic condition (Fig. 1D), consistent with membrane release and the ability to access different substrates.

These results support a model in which ER confinement maintains persistent small oligomers, while release from the membrane permits the long-range coalescence that produces hyperclusters. Once displaced from the ER, these hyperclusters would no longer be restricted to ER-localized substrates and could instead access cytoplasmic transcript pools, potentially engaging distinct downstream biology.

Fig. 2: Optogenetic activation reveals topology-dependent IRE1α oligomerization and signaling outputs.

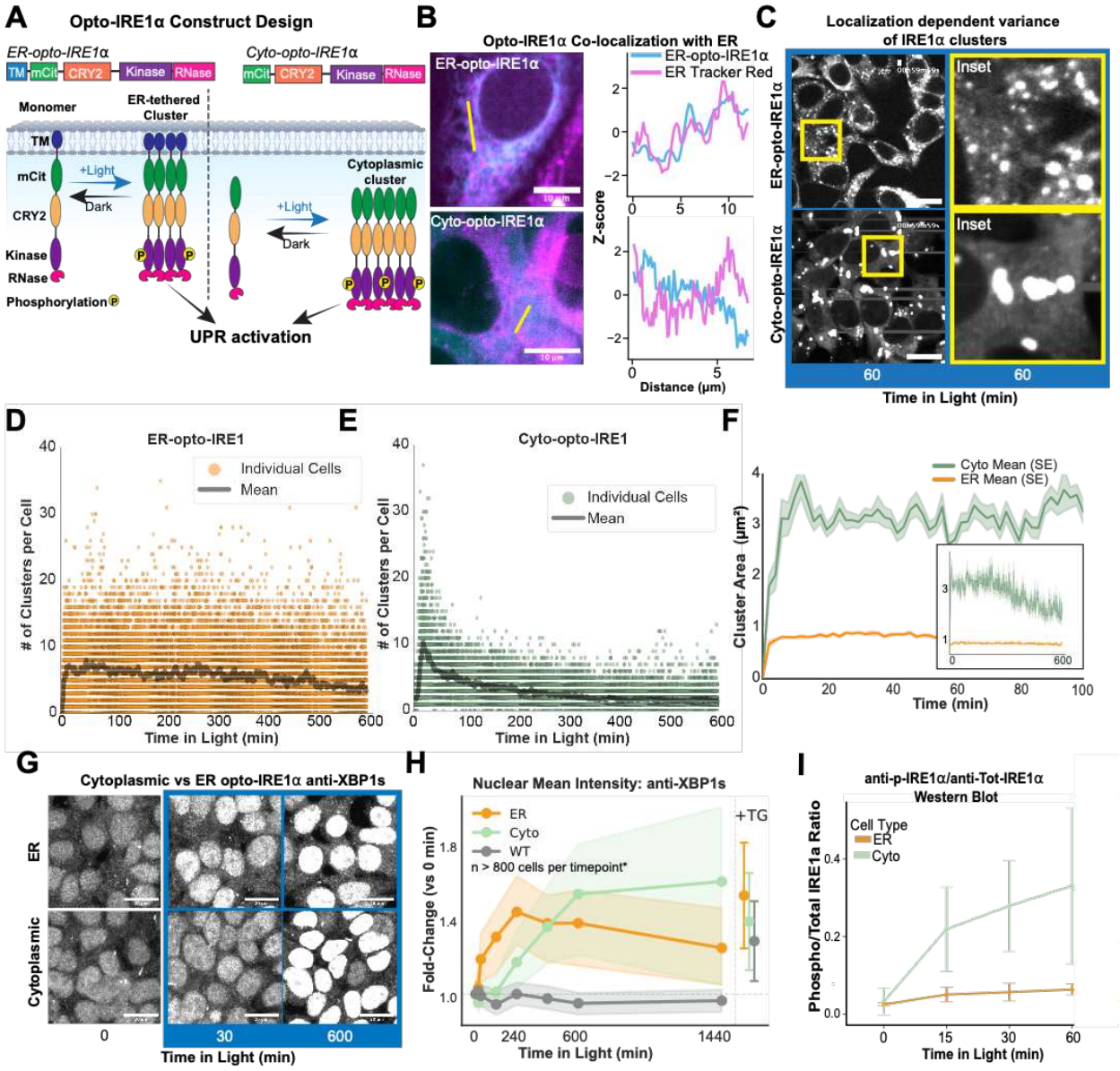


*Figure 2: **(A)** Schematic of the two optogenetic constructs. ER-opto-IRE1α retains the native transmembrane domain and localizes to the ER; Cyto-opto-IRE1α lacks the transmembrane domain and diffuses freely in the cytoplasm. Both fuse the cytosolic kinase-RNase domain of IRE1α to mCitrine-CRY2olig, enabling light-inducible homo-oligomerization upon 450 nm illumination. **(B)** Representative confocal images of stable HEK293T ER- and Cyto-opto-IRE1α cells co-stained with ER-Tracker Red, confirming correct subcellular localization. Right: z-scored mean intensity line profiles demonstrating co-localization (ER-opto-IRE1α) or exclusion (Cyto-opto-IRE1α) from the ER. Scale bars, 10 μm. **(C)** Representative live-cell confocal images of HEK293T ER- and Cyto-opto-IRE1α cells after 60 min of continuous 450 nm illumination, illustrating small persistent clusters (ER) versus large hyperclusters (Cyto). Scale bars, 20 μm. **(D, E)** Quantification of cluster counts per cell over 10 h of continuous illumination for ER-opto-IRE1α (D) and Cyto-opto-IRE1α (E) in HEK293T cells. The black line is the mean of individual cells from a single time-lapse (Supplementary Video 4). **(F)** Cluster area quantification for ER- and Cyto-opto-IRE1α over the 10 h imaging period. Data shown are mean ± s.e.m. **(G)** Representative immunofluorescence images of HEK293T ER- and Cyto-opto-IRE1α cells stained with anti-XBP1-s antibody at selected time points following illumination. Scale bars, 20 μm. **(H)** Quantification of nuclear anti-XBP1-s mean fluorescence intensity over time in illuminated*

HEK293T ER- and Cyto-opto-IRE1α cells, normalized to dark controls. Data shown are mean ± s.e.m. ***(I)*** *Quantification of phosphorylated IRE1α (S724) normalized to total IRE1α and β-actin from western blots of HEK293T ER- and Cyto-opto-IRE1α cell lysates over time. Data shown are mean ± std of n = 3 biological replicates.*

Optogenetic activation of IRE1α reveals topology-dependent oligomerization and signaling

Our diffusion results predict that ER-tethered and cytoplasmic IRE1α should produce qualitatively different oligomerization dynamics. However, testing this with poisons would convolve damage, activation of the other UPR branches, and cannot control topology independently. We therefore turned to optogenetics. We fused the cytosolic kinase-RNase domain of IRE1α to mCitrine-CRY2olig, which undergoes rapid homo-oligomerization upon 450 nm illumination, and generated two constructs[20]. (1) ER-opto-IRE1α, which retains the native transmembrane domain and localizes to the ER, and (2) Cyto-opto-IRE1α, in which the transmembrane domain is removed so that the protein diffuses freely in the cytoplasm (Fig. 2A). Stable pseudoclonal HEK293T and U2OS lines were established for each construct, and correct localization was confirmed by co-staining with ER-Tracker Red (Fig. 2B). Cyto-opto-IRE1α required approximately 4-fold higher expression than ER-opto-IRE1α to achieve robust clustering, consistent with the higher diffusion coefficient in three dimensions predicted by the Brownian clustering model, and within the range of IRE1α protein accumulation reported during prolonged ER stress[23] (Fig. S2A).

Live-cell imaging over 10 hours of continuous illumination revealed oligomerization kinetics that matched the simulation predictions from Figure 1. ER-opto-IRE1α formed small, persistent clusters that remained stable throughout the imaging period, closely resembling early-timepoint FL-IRE1α-mNG oligomers (Fig. 2C-F, Supplementary Video 4). Cyto-opto-IRE1α, by contrast, rapidly coalesced into one or two large hyperclusters within approximately one hour (Fig. 2C-F). These hyperclusters were morphologically similar to the late-timepoint FL-IRE1α-mNG clusters observed under prolonged thapsigargin treatment. The quantitative agreement between the optogenetic data and the Brownian clustering model, whose parameters were drawn entirely from prior literature rather than fit to these experiments, provides independent support for the conclusion that dimensionality of diffusion is sufficient to explain the divergent clustering phenotypes.

We next asked whether these different oligomeric states produce different signaling outputs. Using the OptoPlate system for precise single-well illumination in 96-well format[24], we activated each construct across time points spanning 0 to 24 hours and stained for canonical IRE1α pathway markers (Fig. 2G-H; Fig. S2B-C). Both constructs induced XBP1-s protein expression in response to light, confirming that the kinase-RNase domain retains splicing activity regardless of topology. However, the kinetics differed markedly. ER-opto-IRE1α produced detectable nuclear XBP1-s within 30 minutes of illumination, whereas Cyto-opto-IRE1α showed a severely delayed response (Fig. 2H). Because XBP1-u mRNA is co-translationally targeted to the ER membrane[14], this difference is consistent with ER-tethered IRE1α having preferential access to its splicing substrate.

The phosphorylation data revealed an unexpected dissociation between kinase activation and RNase output. Western blot quantification of phosphorylated IRE1α (S724) normalized to total IRE1α and β-actin showed that Cyto-opto-IRE1α achieved substantially higher phosphorylation levels than ER-opto-IRE1α at all time points tested (Fig. 2I, Fig. S2D). Immunofluorescence with the same anti-p-IRE1α(S724) antibody confirmed this result and demonstrated that the phosphorylation signal co-localized with cytoplasmic oligomers, verifying that these clusters are catalytically active (Fig. S2B-C, E). Yet despite this elevated phosphorylation, which is canonically associated with enhanced RNase activity, Cyto-opto-IRE1α was slower to produce XBP1-s protein. This dissociation indicates that phosphorylation status alone does not determine RNase output and that substrate access, governed by topology, can be equally determinative.

Both constructs also induced RIDD activity, as assessed by qRT-PCR for the canonical RIDD substrate BLOC1S1 under transcriptional arrest[25] (Fig. S2F). After scaling for total IRE1α expression, ER-opto-IRE1α drove more efficient BLOC1S1 decay per IRE1α molecule than Cyto-opto-IRE1α, again consistent with ER localization facilitating access to ER-proximal transcripts. All signaling readouts, including XBP1-s nuclear intensity, p-IRE1α levels, and CHOP immunofluorescence, were independently replicated in U2OS cells, confirming that the topology-dependent differences are not cell-type specific (Fig. S3).

These results establish that subcellular topology shapes both the oligomeric dynamics and the downstream signaling output of IRE1α. ER tethering produces small, persistent clusters that efficiently access ER-localized substrates, while cytoplasmic diffusion drives hypercluster formation with elevated phosphorylation but reduced access to canonical targets. This raised the question of what transcripts cytoplasmic IRE1α does engage, which we addressed by transcriptomic profiling.

Fig. 3: Transcriptomic analysis of ER- and Cyto-opto-IRE1α reveals that ER release leads to decay of cytoskeletal/adhesion-associated genes and cell cycle arrest.

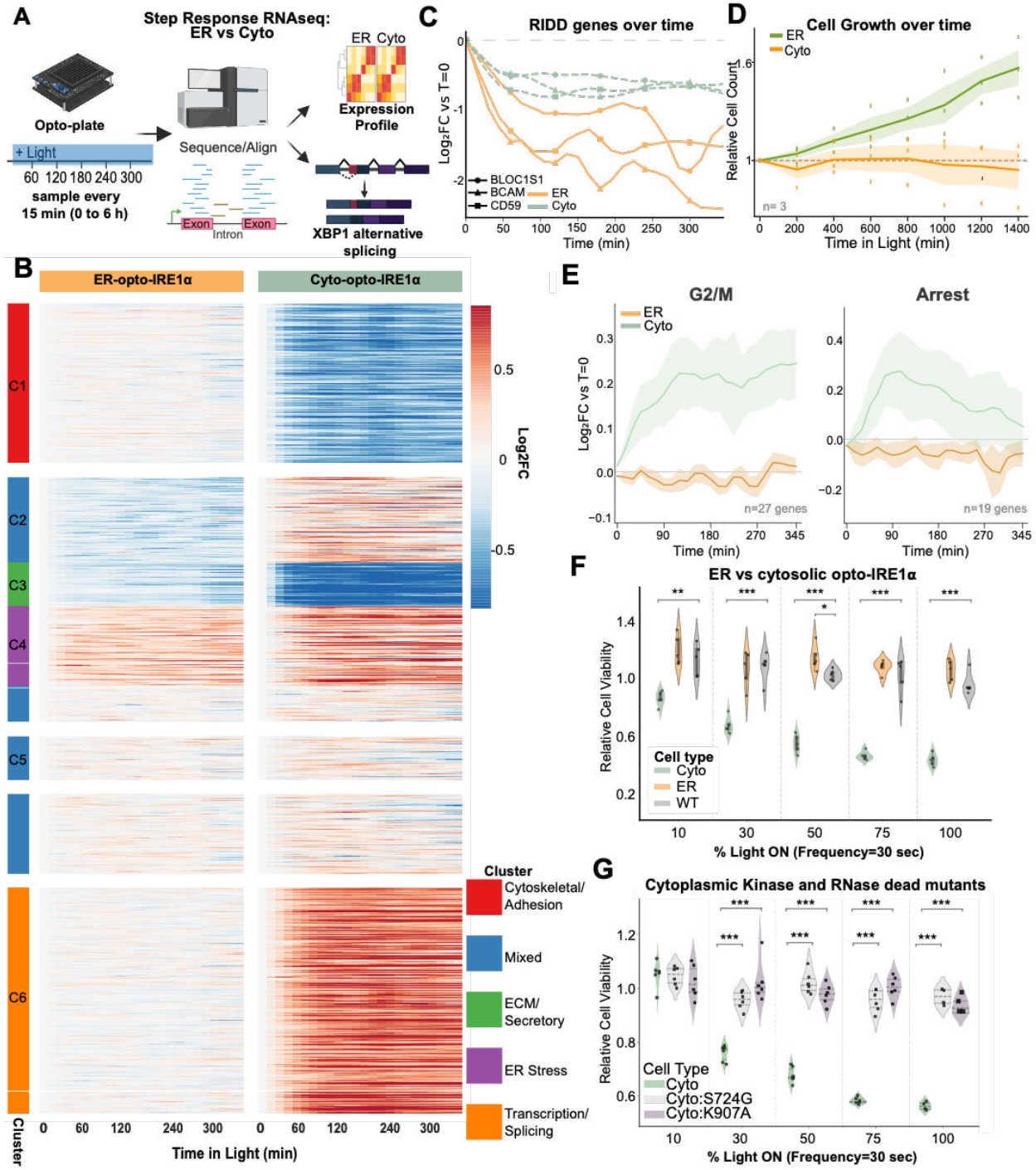


*Figure 3: **(A)** Schematic of the time-series bulk RNA-seq experiment. HEK293T ER- and Cyto-opto-IRE1α cells were illuminated continuously using the OptoPlate system; samples were collected every 15 min over a 345 min time course (n = 48 total samples). **(B)** Genome-wide heatmap of log_2 fold changes relative to t = 0 min, clustered by k-means (k = 6). Cluster annotations reflect the top Gene Ontology Biological Process terms for each cluster. Cluster C1 (cytoskeletal organization, cell adhesion, small*

GTPase signaling). Cluster C3 (secreted/ER-luminal transcripts, canonical RIDD targets). Cluster C2 (spliceosome assembly, RNA processing). ***(C)*** *Expression over time of three individually validated canonical RIDD target transcripts (BLOC1S1, BCAM, CD59) in ER- and Cyto-opto-IRE1α cells. Values are log_2 fold change relative to t = 0 and normalized to anti-total-IRE1α protein levels to correct for the ~4-fold expression difference between constructs.* ***(D)*** *Quantification of cell number over 1,440 min (24 h) of continuous illumination from live-cell imaging of ER- and Cyto-opto-IRE1α cells. Data shown are mean ± s.e.m.; n = 3 replicate wells.* ***(E)*** *Mean log_2 fold change relative to t = 0 of genes associated with G2/M phase and cell-cycle arrest across 345 min of illumination. Shaded area indicates s.e.m.* ***(F)*** *Resazurin cell viability assay comparing wild-type, ER-opto-IRE1α, and Cyto-opto-IRE1α HEK293T cells after 24 h of illumination at increasing light duty cycles (30 s intervals). Viability is normalized to respective dark controls. Data shown are mean ± IQR; n = 5 replicate wells per condition. (Welch's t-test, p < 0.01 = **, p < 0.001 = ***)* ***(G)*** *Resazurin viability assay comparing wild-type Cyto-opto-IRE1α with kinase-dead (S724G) and RNase-dead (K907A) point mutants after 24 h of illumination at a 50% duty cycle. All three constructs form comparable oligomers upon illumination (Supplementary Video 6); neither catalytically inactive mutant reduces viability, establishing that both enzymatic activities are required for growth arrest. Data shown are mean ± IQR; n = 5 replicate wells per condition. (Welch's t-test, p < 0.01 = **, p < 0.001 = ***)*

Cytoplasmic IRE1α activation drives selective decay of cytoskeletal and adhesion transcripts and cell-cycle arrest

To characterize the transcriptional consequences of ER- versus cytoplasmic IRE1α activation with high temporal resolution, we performed time-series bulk RNA-seq using the OptoPlate for single-well illumination control (Fig. 3A). HEK293T ER-opto-IRE1α and Cyto-opto-IRE1α cells were illuminated continuously, with samples collected every 15 minutes over a 345-minute time course (see Methods for sequencing and alignment details).

The two constructs produced strikingly different transcriptional responses. DESeq2 analysis with spline-fitting across the time course identified 5,319 differentially expressed genes (DEGs) in Cyto-opto-IRE1α cells compared with only 651 in ER-opto-IRE1α cells (adjusted $p < 1 \times 10^{-3}$). GO analysis of the top DEGs from each condition confirmed enrichment for canonical ER stress response terms in both, validating that the optogenetic constructs engage the expected pathway (Fig. S4C-D). UMAP of all 48 samples and heatmaps of established IRE1α target genes further confirmed construct-specific activation (Fig. S5A-B, E).

To identify the functional categories underlying this 8-fold difference in DEG number, we generated a genome-wide heatmap of log_2 fold changes relative to the 0-minute time point and applied k-means clustering (optimal k = 6; Fig. 3B). GO analysis of each cluster revealed a clear pattern. Gene clusters upregulated in both constructs were enriched for ER stress response terms, as expected (Fig. 3B). A shared decay cluster (C3, approximately 500 genes) was enriched for luminal, extracellular matrix, and secretory pathway components, consistent with canonical RIDD targets previously reported to be preferentially degraded due to their ER localization[11]. Examination of three individually validated RIDD substrates, BLOC1S1, BCAM, and CD59, confirmed that all three decreased over time in both conditions (Fig. 3C). After normalizing for total IRE1α expression levels (quantified by western blot), ER-opto-IRE1α drove more efficient decay of these transcripts per IRE1α molecule than Cyto-opto-IRE1α, reinforcing the conclusion from Figure 2 that ER localization facilitates access to ER-proximal substrates.

The most prominent topology-dependent difference was a cluster of approximately 2,000 genes (C1) that were selectively downregulated in Cyto-opto-IRE1α but unchanged in ER-opto-IRE1α (Fig. 3B). GO analysis of this cluster revealed enrichment for cytoskeleton organization, cell adhesion, small GTPase signaling, and protein modification, processes collectively associated with cell proliferation. This selective decay persisted after normalizing for the difference in total IRE1α expression between constructs (Fig. S5A), confirming that it reflects a topology-dependent program rather than a simple dosage effect. By contrast, the shared RIDD cluster (C3) showed equivalent decay in both conditions after the same normalization (Fig. S5B), consistent with prior RNA-seq datasets showing that IRE1α selectively degrades secretome-associated transcripts regardless of expression level[11].

A separate cluster of genes was significantly upregulated only in Cyto-opto-IRE1α cells, enriched for spliceosome assembly and RNA processing components (Fig. 3B, S5C). This observation, which we return to in the context of XBP1 alternative splicing (Fig. 5), suggests that cytoplasmic hyperclusters engage RNA processing machinery beyond canonical RIDD.

The broad downregulation of proliferation-associated transcripts in Cyto-opto-IRE1α cells predicted a functional impairment of cell growth. To test this, we performed live-cell imaging of both constructs under continuous illumination for 24 hours (Fig. 3D, S5C, Supplementary Video 5). Cyto-opto-IRE1α cells ceased dividing during the imaging period but, unexpectedly, did not undergo apoptosis. Cells remained attached, maintained membrane integrity, and showed none of the morphological hallmarks of apoptotic death. Western blot analysis confirmed no activation of cleaved caspase-3, caspase-9, or PARP under these conditions (Fig. S5D-E). CHOP immunofluorescence was likewise not induced by illumination of either construct, though thapsigargin treatment robustly activated CHOP as a positive control (Fig. S5F-G). To assess whether genes associated with cell cycle arrest increased over time in Cyto-opto-IRE1α cells, we analyzed phase-specific proliferation gene sets and observed elevated expression of genes linked to the G2/M phase and cell cycle arrest (Fig. 3E). Together, these data indicate that cytoplasmic IRE1α activation drives cell-cycle arrest rather than apoptosis, a phenotype distinct from the terminal UPR outcome typically associated with IRE1α hyper-oligomerization[26].

To quantify this effect, we used a resazurin-based viability assay while varying the light duty cycle at 30-second intervals over 24 hours. Increasing the duty cycle produced a progressive, dose-dependent decrease in viable cell number specifically in Cyto-opto-IRE1α cells, while ER-opto-IRE1α and wild-type cells showed no change relative to dark controls (Fig. 3F). This phenotype was reproduced in U2OS cells (Fig. S4E). To confirm that growth arrest required IRE1α enzymatic activity rather than overexpression or oligomerization per se, we generated expression-matched kinase-dead (S724G) and RNase-dead (K907A) point mutants of Cyto-opto-IRE1α. Both mutants formed large oligomers comparable to the wild-type construct upon illumination (Supplementary Video 6), but neither reduced cell viability (Fig. 3G). Both enzymatic activities are therefore required for the growth arrest phenotype, and oligomerization alone is not sufficient.

Given that cytoplasmic IRE1α engages a distinct transcript decay program and upregulates spliceosome components, we asked whether its processing of XBP1 itself might also differ from the canonical pathway.

Fig. 4: ER release of IRE1α leads to formation of the cryptic XBP1 isoform, XBP1-es, leading to a decoupling of ISR-related genes.

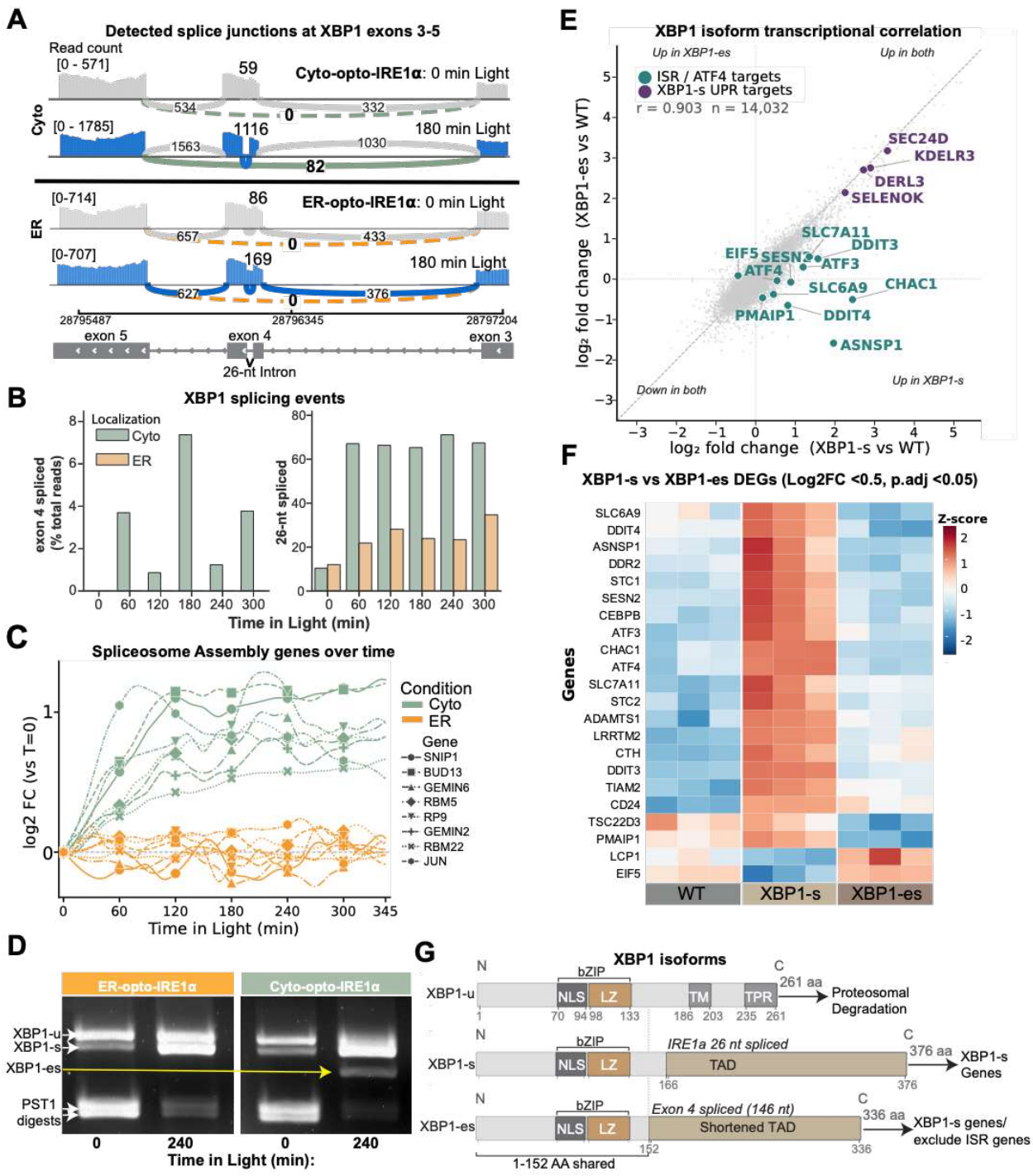


Figure 4: ***(A)*** *IGV sashimi plots of the XBP1 locus from time-series RNA-seq data showing junction reads spanning exon 3–exon 4, exon 4–exon 5, and exon 3–exon 5 for ER- and Cyto-opto-IRE1α cells. Exon 3–exon 5 junction reads are present in all illuminated Cyto-opto-IRE1α samples and absent from all ER-opto-IRE1α time points.* ***(B)*** *Quantification of percent-spliced-in (PSI) values for the canonical 26-nt IRE1α-mediated intron (XBP1-s) and the exon 4-skipping event (XBP1-es) across time points in ER- and Cyto-opto-IRE1α cells. Data are derived from junction read counts in the RNA-seq dataset.* ***(C)*** *Spliceosome assembly genes Log_2 Fold Changes to dark controls*

over time from step response bulk RNA-seq (Smoothing performed using 3-point boxcar uniform filter). ***(D)*** *RT-PCR of the XBP1 amplicon spanning exon 4 in ER- and Cyto-opto-IRE1α cells after 4 h of illumination, followed by PstI digestion. An additional amplicon migrating below XBP1-s is present exclusively in Cyto-opto-IRE1α samples; Sanger sequencing confirmed this band as the exon 4-skipped isoform (XBP1-es).* ***(E)*** *Scatterplot comparing log_2 fold changes of all expressed genes between doxycycline-induced XBP1-s and XBP1-es in stable HEK293T lines versus doxycycline-treated wild-type controls. The majority of genes are co-regulated by both isoforms; the 20 genes elevated exclusively in XBP1-s cells (highlighted) are enriched for integrated stress response (ISR) components, including ATF4 and CHOP.* ***(F)*** *Z-scored heatmap of the 22 differentially expressed genes between XBP1-s and XBP1-es conditions (adjusted $p < 0.05$, $|log_2FC| > 0.5$). Twenty genes are upregulated in XBP1-s and remain at wild-type levels in XBP1-es, including the two central ISR effectors ATF4 and DDIT3/CHOP.* ***(G)*** *Schematic of XBP1 isoforms. XBP1-u: unspliced; XBP1-s: IRE1α-spliced (26-nt intron removal within exon 4); XBP1-es: exon 4-skipped isoform generated by spliceosome-mediated alternative splicing. Domain annotations: TM, transmembrane domain; TAD, transactivating domain; bZIP, basic leucine zipper.*

Cytoplasmic IRE1α activation generates XBP1-es, an exon 4-skipped isoform that decouples IRE1α signaling from the integrated stress response

We next compared how the XBP1 mRNA processing between ER-tethered and cytoplasmic hyperclustering IRE1α. Analysis of junction reads across the XBP1 locus at six time points (0, 60, 120, 180, 240, and 300 minutes of illumination) confirmed the expected increase in reads lacking the canonical 26-nucleotide intron within exon 4, the hallmark splicing event that generates XBP1-s, in both ER- and Cyto-opto-IRE1α cells (Fig. 4A-B). However, all illuminated Cyto-opto-IRE1α samples also contained reads in which the entirety of exon 4 was skipped (Fig. 4A-B, Fig. S6A-B). This junction was absent from every ER-opto-IRE1α time point.

This exon-skipped variant, termed XBP1-es, was previously described in chimpanzee cells during rotavirus infection, where it was shown to retain transcription factor activity on UPR target promoters[27]. In that study, IRE1α inhibition did not prevent XBP1-es formation, and thapsigargin treatment alone did not produce it, leading the authors to conclude that XBP1-es arises through spliceosome-mediated exon skipping rather than direct IRE1α RNase activity. To our knowledge, XBP1-es has not been reported in human cells in the context of ER stress. Our data demonstrate that cytoplasmic IRE1α oligomerization is sufficient to induce XBP1-es, connecting this isoform to IRE1α activity for the first time. Because cytoplasmic IRE1α activation also upregulates spliceosome assembly genes (Fig. 3B, 4C), we propose that IRE1α does not catalyze the exon-skipping event directly but instead alters the splicing environment in a manner that promotes the alternative splicing of XBP1 mRNA to produce XBP1-es.

To validate XBP1-es, we performed RT-PCR spanning the XBP1 locus followed by PstI digestion[21] in cells illuminated for 4 hours (Fig. 4D). Both constructs showed the expected increase in the XBP1-s amplicon. Cyto-opto-IRE1α samples contained an additional band migrating below XBP1-s that was absent from ER-opto-IRE1α samples. This band was gel-extracted and confirmed by Sanger sequencing to correspond to the exon 4-skipped isoform.

We next asked whether XBP1-es has functional consequences distinct from canonical XBP1-s. To compare their transcriptional programs, we cloned XBP1-s-mCitrine and XBP1-es-mCitrine into a doxycycline-inducible lentiviral backbone and generated stable HEK293T lines. After 24 hours of doxycycline induction, we performed bulk RNA-seq in triplicate alongside doxycycline-treated wild-type controls (Fig. 4E-G, S7). The two isoforms drove remarkably similar transcriptional responses: the top four upregulated GSEA hallmark terms were identical, PCA

placed all XBP1-s and XBP1-es samples along the same PC1 axis (accounting for approximately 95% of variance), and the global correlation between their DEG profiles was high (Fig. 4E, S7). XBP1-es therefore retains broad transcription factor activity across the canonical UPR target gene set.

Only 22 genes were differentially expressed between XBP1-s and XBP1-es (adjusted $p < 0.05$, $\log_2$ fold change > 0.5), and 20 of these were elevated in XBP1-s cells while remaining at wild-type levels in XBP1-es cells (Fig. 4E-F). The majority of these 20 genes belonged to the integrated stress response, including ATF4 and DDIT3 (CHOP), the two central transcriptional effectors of the PERK/eIF2α/ATF4 axis. XBP1-es therefore functions as a UPR transcription factor that selectively fails to engage the ISR, effectively decoupling IRE1α output from the PERK/ATF4/CHOP program (Fig. 4G). This result identifies exon 4 as the domain through which XBP1-s intersects with ISR gene induction.

To assess whether XBP1-es is present in human tumors, we queried RNA-seq junction data from 11,237 TCGA samples using the Snaptron database[28] (Fig. S6D). Exon 3-to-exon 5 junction reads consistent with XBP1-es were detected in 10.9% of tumors, with the highest prevalence in acute myeloid leukemia (LAML, 60%) and breast cancer (BRCA, 27%). Both malignancies are characterized by elevated ER stress and high rates of caspase activation during disease progression[9,29], conditions that could produce the caspase-mediated IRE1α cleavage described by Harnoss et al. and thereby generate the free cytoplasmic kinase-endonuclease domain. The enrichment in LAML is particularly notable, as leukemic cells undergo continuous apoptotic turnover with sustained caspase activity[30,31], providing a plausible mechanism for chronic IRE1α displacement from the ER. These observations raise the possibility that XBP1-es serves as a molecular marker of cytoplasmic IRE1α activity in tumors where stress or apoptotic priming permits non-canonical IRE1α signaling.

Fig. 5: PAIR2 blocks cytoplasmic IRE1α hypercluster formation and rescues cell cycle arrest while preserving XBP1 splicing and selective RIDD.

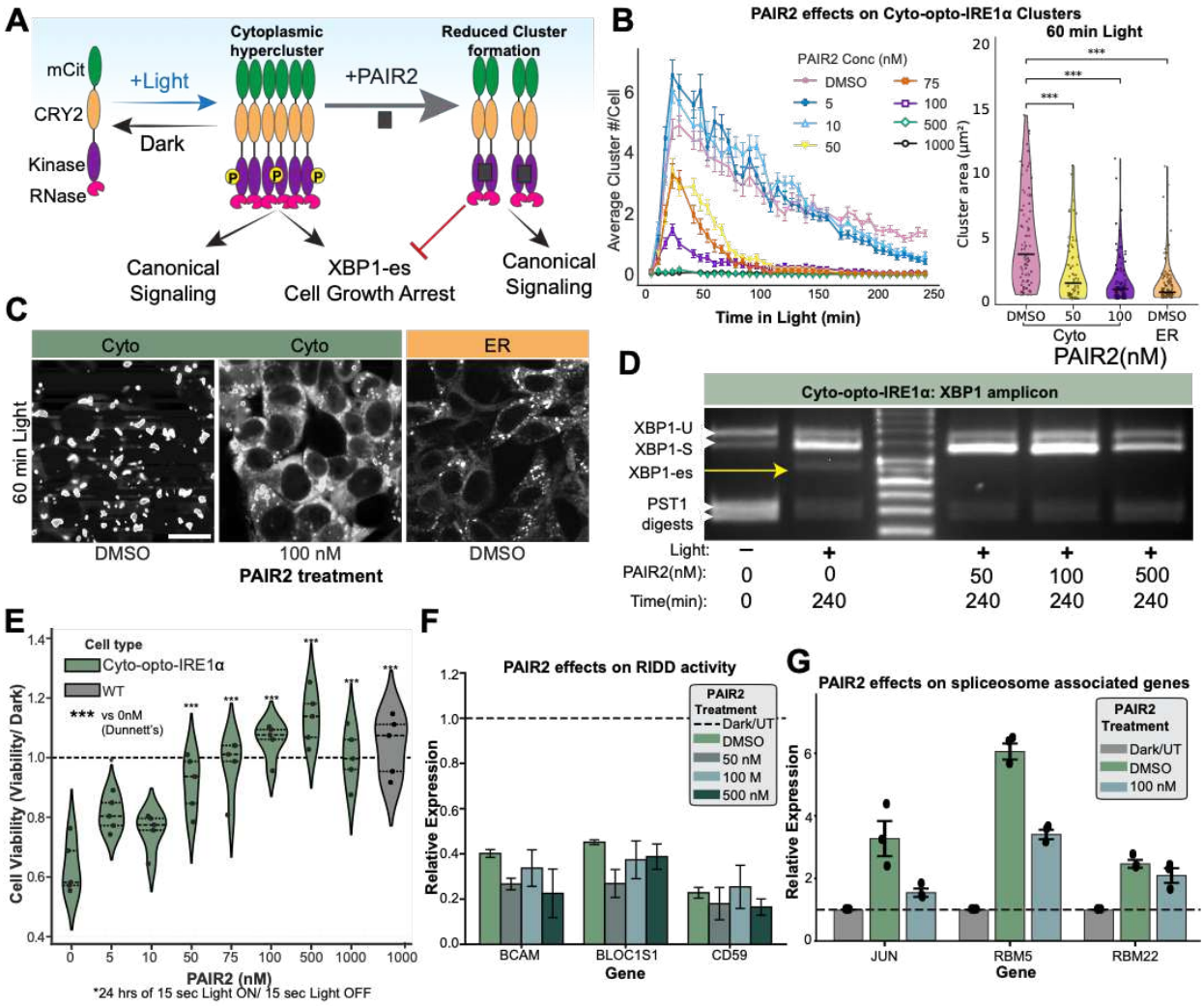


Figure 5: ***(A)*** *Schematic illustrating the mechanism of PAIR2 action. PAIR2 is an ATP-competitive partial antagonist of the IRE1α kinase domain that stabilizes an intermediate helix-αC conformation, selectively blocking high-order oligomerization (hyperclusters) while preserving lower-order dimeric/trimeric assemblies sufficient for adaptive XBP1 splicing and RIDD.* ***(B)*** *Quantification of Cyto-opto-IRE1α cluster count and mean cluster area over time in the presence of increasing PAIR2 concentrations (5–1,000 nM) compared with DMSO controls. At ≥ 1,000 nM, PAIR2 completely prevents hypercluster formation. Data shown are mean ± s.e.m. of individual cells from a single time-lapse experiment. (Kruskal-Wallis test, $p < 0.001$ = ***)* ***(C)*** *Representative confocal images of Cyto-opto-IRE1α cells treated with DMSO or 100 nM PAIR2, and ER-opto-IRE1α cells treated with DMSO, after 60 min of illumination. PAIR2 abolishes cytoplasmic hyperclusters without affecting ER-anchored cluster formation. Scale bars, 20 μm.* ***(D)*** *RT-PCR of the XBP1 amplicon in Cyto-opto-IRE1α cells after 240 min of illumination in the presence of increasing PAIR2 concentrations.* ***(E)*** *Resazurin cell viability assay of Cyto-opto-IRE1α cells illuminated at a 50% duty cycle for 24 h in the presence of increasing PAIR2 concentrations. Growth arrest is dose-dependently rescued; 100 nM PAIR2 restores viability to levels indistinguishable from dark controls. Data shown are mean ± s.e.m.; n = 5 replicate wells per condition. (Dunnett's test vs 0 nM PAIR2, $p < 0.001$ = ***)* ***(F)*** *qRT-PCR of canonical RIDD target transcripts BLOC1S1, BCAM, and CD59 in Cyto-opto-IRE1α cells illuminated for 4 h in the presence of 50, 100, or 500 nM PAIR2 or DMSO. Data shown are mean ± s.e.m. of n = 3 replicates.* ***(G)*** *qRT-PCR of spliceosome-associated and stress-signaling transcripts JUN, RBM5, and RBM22 in Cyto-opto-*

IRE1α cells in the presence of increasing PAIR2 concentrations after 4 h of illumination. Data shown are mean ± s.e.m. of n = 3 replicates.

Pharmacological dissection with PAIR2 separates adaptive IRE1α outputs from the growth arrest program

The results above show that cytoplasmic IRE1α hyperclusters drive growth arrest, RIDD, XBP1 splicing, and XBP1-es formation simultaneously. To determine which of these outputs require hypercluster formation, we turned to PAIR2, an ATP-competitive antagonist that binds the IRE1α kinase pocket and selectively inhibits hyper-oligomerization while preserving adaptive RNase activity[21] (Fig. 5A).

We first confirmed that PAIR2 suppresses cytoplasmic hypercluster formation. At concentrations above 1,000 nM, PAIR2 completely prevented Cyto-opto-IRE1α oligomerization upon illumination, while ER-opto-IRE1α clustering was unaffected at all concentrations tested (Supplementary Video 7). Dose-response imaging across a 5 to 1,000 nM range revealed that cluster counts began to decline above 50 nM and that existing clusters disassembled more rapidly in the presence of PAIR2 (Fig. 5B-C; Supplementary Video 8). PAIR2 therefore selectively targets the cytoplasmic hypercluster without disrupting ER-tethered oligomers.

With hypercluster formation suppressed, we asked which downstream outputs persisted and which were lost. We assessed three categories: canonical RNase outputs (XBP1 splicing and RIDD), the growth arrest phenotype, and the non-canonical outputs (XBP1-es and spliceosome gene induction).

Canonical RNase outputs were preserved. RT-PCR of the XBP1 amplicon after 240 minutes of illumination showed that XBP1 splicing persisted even in the presence of 500 nM PAIR2 (Fig. 5D). qRT-PCR for the canonical RIDD substrates BLOC1S1, CD59, and BCAM confirmed that transcript degradation continued at 50, 100, and 500 nM PAIR2 (Fig. 5F). RIDD activity therefore does not require hypercluster formation and can proceed from lower-order oligomeric states that persist in the presence of PAIR2. This result carries a direct mechanistic implication: because PAIR2 fully rescued proliferative capacity while RIDD remained active, RIDD alone is insufficient to drive growth arrest. This challenges the prevailing view that RIDD is a primary mediator of adverse IRE1α signaling outcomes and instead points to a kinase-dependent output, accessible through the PAIR2-sensitive pocket, as the driver of the arrest phenotype.

Growth arrest was fully reversed in Cyto-opto-IRE1α cells illuminated at a 50% duty cycle for 24 hours in the presence of increasing PAIR2 concentrations showed dose-dependent rescue of viability, with even 5 nM producing a measurable improvement and 100 nM restoring proliferation to levels indistinguishable from dark controls (Fig. 5E).

Non-canonical outputs were abolished. In contrast to canonical XBP1 splicing, XBP1-es was completely absent at PAIR2 concentrations as low as 50 nM (Fig. 5D). This finding is particularly informative when compared with prior work showing that the RNase inhibitor STF-083010 did not prevent XBP1-es formation during viral infection[27], because it implies that XBP1-es requires a hypercluster-associated signaling state rather than RNase catalysis per se. Consistent with this interpretation, qRT-PCR showed that PAIR2 also suppressed the induction

of JUN and the spliceosome-associated genes RBM5 and RBM22 (Fig. 5F), all of which were upregulated selectively in Cyto-opto-IRE1α cells in the transcriptomic analysis (Fig. 3B, 4C). JUN is activated downstream of JNK phosphorylation and has been shown to interact with the splicing regulator RBM39 to influence alternative splicing decisions[32], providing a potential link between kinase-dependent signaling within cytoplasmic hyperclusters and the altered splicing environment that produces XBP1-es.

Taken together, the PAIR2 experiments pharmacologically decompose cytoplasmic IRE1α signaling into two separable programs: an adaptive module comprising XBP1 splicing and RIDD that operates from lower-order oligomers and does not require the kinase pocket, and an arrest-associated module comprising growth arrest, XBP1-es formation, and spliceosome engagement that requires hypercluster formation and is sensitive to kinase-pocket occupancy. The topology of IRE1α determines which of these programs is engaged, with ER confinement restricting signaling to the adaptive module and cytoplasmic release licensing the full repertoire.

Discussion

Two physical consequences follow when IRE1α's kinase/RNase domains are displaced from the ER. First, the RNase has reduced access to its canonical ER-localized substrates, XBP1-u mRNA and RIDD targets, and gains access to cytoplasmic transcript pools. Second, the kinase/RNase domain is freed from the lateral constraints of a two-dimensional membrane, enabling both higher-order oligomerization (as predicted by our Brownian clustering model and confirmed by live imaging) and elevated trans-autophosphorylation (as measured by S724 phosphorylation). Either or both of these changes could rewire signaling output. Our data indicate that they act in concert to produce a signaling program that is qualitatively distinct from canonical ER-tethered IRE1α: one characterized by widespread cytoskeletal and adhesion transcript decay, cell-cycle arrest without apoptosis, and the generation of XBP1-es, an isoform that selectively decouples IRE1α output from the integrated stress response.

This distinction between ER-tethered and cytoplasmic IRE1α outputs challenges two assumptions of the current oligomerization model. The first is that phosphorylation intensity predicts RNase output. Cyto-opto-IRE1α achieved substantially higher S724 phosphorylation than ER-opto-IRE1α, yet was slower to produce XBP1-s protein, because XBP1-u mRNA is co-translationally targeted to the ER membrane and is poorly accessible to a cytoplasmic enzyme[14]. Topology, therefore, imposes a substrate-access filter that can override the phosphorylation-activity relationship. The second assumption is that RIDD mediates the adverse outcomes of IRE1α hyper-oligomerization. The PAIR2 experiments dissociate these two outputs pharmacologically: at concentrations that fully rescued proliferative capacity, canonical RIDD substrates continued to be degraded. The growth arrest phenotype instead requires a kinase-dependent output accessible through the PAIR2-sensitive ATP-binding pocket, a conclusion reinforced by the failure of kinase-dead Cyto-opto-IRE1α to reduce viability despite forming comparable oligomers. Identifying the cytoplasmic substrates of this kinase activity is an important open question.

The most far-reaching implication of this work may be the identification of XBP1-es as a topology-gated isoform that functionally separates IRE1α signaling from the PERK/ATF4/CHOP axis. In the canonical UPR, the balance between the IRE1α and PERK

branches determines cell fate: sustained PERK activation drives ATF4 and CHOP expression, committing cells to apoptosis, while sustained IRE1α/XBP1-s activity promotes proteostatic adaptation and survival[8,23]. These two branches are coupled in part through XBP1-s itself, as our data show that 20 of 22 genes differentially expressed between XBP1-s and XBP1-es belong to the ISR, with ATF4 and DDIT3/CHOP among them. XBP1-es retains the ability to drive the full canonical UPR target gene set, including chaperones and ERAD components, but specifically fails to engage this ISR-coupled gene program. The functional consequence is a transcription factor that provides the adaptive benefits of XBP1-s, enhanced protein folding capacity, ER expansion, and secretory pathway support, without activating the death-associated arm of the stress response. In effect, XBP1-es creates a third signaling state beyond the classical binary of adaptive UPR versus terminal UPR: a state in which cells can maintain proteostatic competence while being insulated from ISR-induced apoptotic commitment.

This property makes XBP1-es a candidate mechanism for how cancer cells rewire their stress signaling. Tumor cells with high secretory burden or rapid proliferation experience chronic ER stress and depend on IRE1α/XBP1-s activity for survival, but sustained XBP1-s expression also induces pro-apoptotic programs[33]. In AML, sustained XBP1-s drives apoptosis through a miR-22/SIRT1 axis, and XBP1-s ratios correlate with poor survival[34]. A version of XBP1 that retains proteostatic transcription factor activity while dropping the ISR-linked death program would allow leukemic cells to manage their protein-folding burden without triggering the apoptotic consequences of full XBP1-s signaling. The 60% prevalence of XBP1-es junction reads in LAML is consistent with this possibility. LAML is characterized by continuous apoptotic turnover with sustained caspase activity, providing the caspase-mediated IRE1α cleavage[15] that would generate the free cytoplasmic kinase-endonuclease fragment modeled by our Cyto-opto-IRE1α construct. The 27% prevalence in breast cancer, another malignancy with high ER stress burden and frequent caspase activation, fits the same pattern. We propose that XBP1-es junction reads in tumor RNA-seq data may serve as a molecular footprint of cytoplasmic IRE1α activity, and that tumors enriched for XBP1-es may represent a distinct biological subset in which IRE1α signaling has been co-opted for stress adaptation without apoptotic signaling.

If this model is correct, tumors that depend on XBP1-es for ISR-decoupled proteostasis could be vulnerable to interventions that restore the IRE1α-ISR coupling. Our PAIR2 data provide a proof of concept that the hypercluster-dependent and adaptive outputs of IRE1α are pharmacologically separable. PAIR2 abolished XBP1-es at concentrations that preserved canonical XBP1 splicing and RIDD. In the optogenetic system, this separation relieved growth arrest. In a tumor context, however, the consequences of eliminating XBP1-es may differ. If cancer cells use XBP1-es to maintain chaperone and ERAD gene expression while avoiding the pro-apoptotic ISR program that sustained XBP1-s engages (including the miR-22/SIRT1 axis active in AML), then blocking XBP1-es formation would force cells to rely on canonical XBP1-s as their sole UPR transcription factor, re-exposing them to ISR-mediated death. Whether PAIR2-like compounds would be cytotoxic or cytoprotective in specific tumor contexts will depend on which program, XBP1-es-mediated ISR decoupling or hypercluster-associated growth arrest, is the dominant phenotype in vivo, and this is likely to vary by tumor type and disease stage.

XBP1-es is not the only non-canonical XBP1 variant with disease relevance. He et al. identified XBP1v1 (Xv1), a distinct alternatively spliced isoform upregulated in multiple myeloma that

drives a transcriptional program largely non-overlapping with XBP1-s[35]. The recurrence of non-canonical XBP1 isoforms in hematological cancers with chronic ER stress suggests that XBP1 isoform diversity may be a common feature of tumors that must manage sustained proteotoxic burden, rather than a rare aberration. Whether XBP1-es and Xv1 represent convergent solutions to the same selective pressure, or engage different downstream programs, will require direct comparison of their target gene sets.

Although cytoplasmic IRE1α activation is unlikely to represent the dominant signaling mode during acute ER stress, multiple physiological and pathological contexts produce the conditions for it. Caspase-mediated cleavage, ZIKV-induced relocalization to viral replication complexes, and prolonged unresolved ER stress can all displace IRE1α from the ER[15–17]. Our data suggest that this displacement does not inactivate IRE1α but instead redirects it toward a program that includes decay of cytoskeletal and adhesion transcripts, engagement of the spliceosome, and production of an XBP1 isoform that insulates cells from the ISR. Whether this redirection represents a protective adaptation, a maladaptive consequence of sustained stress, or, in the case of cancer, a co-opted survival mechanism may depend on the specific disease context.

Several limitations should be noted. ER- and Cyto-opto-IRE1α were expressed at different levels, with Cyto-opto-IRE1α requiring approximately 4-fold higher expression for robust clustering. However, the lower-expressing ER-opto-IRE1α construct produced XBP1-s more efficiently, arguing against expression level as the driver of signaling differences. IRE1α-scaling normalization of the RNA-seq data confirmed that the topology-dependent decay cluster persisted after correction, and the expression levels used fall within the range of endogenous IRE1α accumulation during prolonged ER stress[23]. The XBP1-es junction reads detected in TCGA, while present in a substantial fraction of samples, were low in absolute abundance per sample; deeper sequencing or targeted assays will be needed to quantify XBP1-es protein levels in patient tumors and to establish whether XBP1-es abundance correlates with clinical outcome.

In summary, this work establishes subcellular topology as a determinant of IRE1α signaling fate that operates alongside and independently of oligomeric state. The combination of optogenetic topology control with pharmacological dissection by PAIR2 reveals two separable IRE1α signaling programs whose engagement is gated by whether IRE1α resides on the ER membrane or in the cytoplasm. The identification of XBP1-es as a topology-dependent isoform that decouples IRE1α output from the ISR, its detection in human cancers characterized by caspase-mediated IRE1α displacement, and the demonstration that this decoupling is pharmacologically reversible together connect the spatial biology of a stress sensor to a potential therapeutic vulnerability in ER stress-adapted tumors.

Methods:

Cell Culture:

HEK293T, U2OS, SNB-19, and EKVX cells were cultured in Dulbecco's Modified Eagle Medium (DMEM) supplemented with 10% fetal bovine serum (FBS; Atlas Biologicals, F-0500-D) and 1% penicillin at 37°C and 5% CO2. Optogenetic cell lines were maintained in the dark and wrapped in foil to prevent light exposure. Passaging of optogenetic lines was performed exclusively under red light conditions to avoid premature activation.

DNA Constructs:

Constructs were created by amplifying the DNA regions of interest from plasmids containing these sequences using PCR with either Primestar MAX or Primestar GXL polymerase premixes using custom primers from IDT. The PCR products were subcloned into lentiviral plasmids containing an SFFV promoter using Gibson assembly, per the manufacturer's instructions. To create the point mutation plasmids, we used custom primers to introduce point mutations via PCR using Primestar GXL. Resulting plasmids were verified using Plasmidsaurus whole plasmid sequencing.

Lentivirus Production:

Cells were seeded in 6-well plates at approximately 30-40% confluence and allowed to attach overnight. On Day 1, fresh media was added, and cells were transfected using polyethyleneimine (PEI) with the following plasmids: psPAX2 (1.7 µg), pMD2.G (0.55 µg), and the lentiviral construct (~2 µg for each 10.5 Kbp plasmid). Forty-eight hours post-transfection, the first viral harvest was performed by filtering the supernatant through a 0.45 µm filter, and the collected virus was stored at 4°C overnight. After the first harvest, fresh media was added to the cells to allow further virus production. Seventy-two hours post-transfection, a second viral harvest was performed in the same manner as the first. The virus was concentrated using LentiX (Takara-Bio) according to the manufacturer's protocol, followed by a 30-minute incubation at 4°C. After incubation, the viral supernatant was centrifuged at 1500g for 45 minutes at 4°C. The resulting pellet was resuspended in 1/10th of the original harvest volume, aliquoted, and stored at -80°C for future use.

Lentivirus Transduction:

Cells were seeded in 6-well plates at approximately 30-40% confluence and allowed to attach overnight. On the following day, transduction was performed using Polybrene at a final concentration of 8 µg/mL in DMEM. Lentivirus was thawed on ice and added dropwise to the cells. The cells were then centrifuged at 1500g for 90 minutes at 32°C to enhance transduction efficiency. After centrifugation, the media was replaced with fresh DMEM, and transduction efficiency was assessed 48 hours later using confocal microscopy.

Pseudo-clone Sorting:

Transduced cells were sorted using the SONY SH-800 cell sorter. Gating was established using non-transduced parental cells as a negative control. For opto-IRE1α-expressing cell lines, three distinct expression levels, low, medium, and high, were sorted. Each expression level was subsequently validated for the most efficient activation of the downstream pathway.

Immunofluorescence:

Cells were plated at a density of 10-20K cells/well in fibronectin-coated glass-bottom 96-well plates (Cellvis, P96-1.5H-N). For HEK293T cells, which exhibit lower adhesion, glass plates were pre-coated for 1 hour in 37C incubators and air-dried for 30 minutes prior to plating. For fixation, 4% paraformaldehyde (PFA; Fisher Scientific, AA433689L) was diluted in DPBS, with a 2X 8% PFA stock used for HEK293T cells to prevent cell detachment. Following fixation, cells were washed with DPBS and permeabilized with blocking buffer (0.05% saponin, 0.5% BSA, 50 mM NH4Cl in PBS) for 1 hour at room temperature. After removal of the blocking buffer, cells were incubated with primary antibodies, diluted in blocking buffer, for 20–27 hours at 4°C, in the dark. After three washes with PBS-T, secondary antibodies were applied for 1 hour at room temperature, followed by 3 additional washes and maintenance in 100 uL of DPBS until imaging.

Microscopy:

Live-cell imaging was performed using a W2 SoRa spinning-disk confocal microscope equipped with an electron-multiplying charge-coupled device (EMCCD) camera (Andor, DU-888) and a 60X NA 1.2 water immersion objective. Time-lapse imaging was conducted at 37°C and 5% CO2. For cell growth live-cell imaging experiments, we used a 20x objective, and CRY2olig activation was performed using the 450nm laser. For cluster tracking of FL-$IRE1\alpha$-mNG in SNB-19 cells, we imaged every 5 seconds using the 450nm laser until mNG bleached at 4-5 hours post-TG and approximately 24 hours post-TG addition. Cluster segmentation and tracking was performed using Fiji/Trackmate (Fig. S1D). Fixed-cell imaging was performed using the CellVoyager CQ1 (Yokogawa) with a CSU W-1 confocal spinning disk system. Maximum Intensity Projection (MIP) of 6 Z-slices with a range of 10 μm were used for all quantifications of fixed images.

FL- IRE1α-mNG cluster tracking:

For the tracking of single FL-IRE1α-mNG clusters in response to ER stress, we acquired images with the 60x NA 1.2 water-immersion objective and the 488 nm laser every 5 sec. This allowed imaging of clusters for ~3 min before bleaching. Images were then processed using Fiji to run background subtraction and Bleach correction. Output timelapses were then segmented for clusters using the Trackmate Thresholding cluster detection method, and tracked using the LAP Tracker. Final output CSVs were drift-corrected to account for whole-cell movements before quantifying MSD, D, and α.

Cluster segmentation and quantifications:

Fluorescence images of opto-*IRE1α* expressing cells (Cyto, and ER) were analyzed using a semi-automated pipeline. Single cells were segmented using custom-trained models in Cellpose (v2), and the resulting masks were used to extract per-cell fluorescence signals in MATLAB. Condensates were identified using different complementary detection modes to capture diverse morphologies. Combined local adaptive thresholding and global thresholding, followed by size filtering and distance transform-based watershed segmentation were used to resolve closely spaced clusters. Detection of high-intensity condensates were done using a maximum intensity threshold with morphological dilation and geometric filtering. Candidate condensates were filtered using constraints on area, mean intensity, maximum-to-mean intensity ratio to exclude noise and non-specific signal. For each condensate, area, circularity, mean intensity, Feret diameter, and intensity variability were quantified, alongside per-cell metrics including total intensity, mean intensity, and cell area. Cells lacking detectable condensates were retained with NaN values to avoid sampling bias. Outputs were exported with corresponding overlay visualizations for quality control.

Manders' Overlap Coefficient Analysis:

FL-IRE1α-mNG SNB-19 cells were treated with 300 nM Thapsigargin (TG) and imaged at 4 h (n = 44 cells, 12 fields of view) and 24 h (n = 30 cells, 20 fields of view). Multi-channel 16-bit TIFF images were acquired with three channels: ER-Tracker Red, FL-IRE1α-mNG, and NucBlue. Whole-cell masks were generated using Cellpose v4.1.1 (CPSAM model), and cytoplasm regions were defined by subtracting the nucleus mask (with 2 px erosion at the boundary) from the cell body mask. Per-image background was estimated as the median intensity of unsegmented cytoplasm pixels and subtracted independently for each channel. The Manders' Overlap Coefficient (MOC) was computed for each cell over all cytoplasm pixels as: $MOC = \Sigma(CH1_i \times CH2_i) / \sqrt{[\Sigma(CH1_i^2) \times \Sigma(CH2_i^2)]}$, where CH1 and CH2 denote background-subtracted ER-Tracker Red and IRE1α-mNG pixel intensities, respectively, and the sum runs over all cytoplasm pixels *i*. MOC ranges from 0 to 1, where values approaching 1 indicate strong spatial overlap independent of relative signal intensities. Cells were excluded if the cytoplasm area was < 200 px² or if segmentation revealed merged nuclei or edge fragments. Group differences in MOC were assessed using the two-sided Mann–Whitney U test; results are reported as median [IQR]. MOC values were 0.765 [0.711, 0.828] at 4 h and 0.562 [0.493, 0.674] at 24 h ($p < 0.0001$). Analysis was performed in Python 3 using NumPy, SciPy, scikit-image, Cellpose, and Matplotlib.

Brownian Clustering Simulation:

Model Overview:

We developed a coarse-grained Brownian dynamics simulation to investigate how anomalous diffusion arising from ER membrane confinement influences IRE1α oligomerization kinetics. The simulation models IRE1α molecules as point-like particles that undergo Brownian motion and merge irreversibly upon contact, representing optogenetically induced CRY2olig-mediated clustering. Two conditions are simulated in parallel: (1) ER-tethered IRE1α, confined to a two-dimensional membrane with ER corral boundaries, and (2) cytoplasmic IRE1α, diffusing freely in a three-dimensional volume. Both simulations use identical interaction rules; they differ only in the dimensionality and transport properties of the diffusive environment.

Simulation Domain and Initial Conditions:

Each simulation begins with N = 200 IRE1α monomers. For the ER-tethered condition, particles are placed randomly on a 12 × 12 μm² two-dimensional surface representing the ER membrane (z = 0). For the cytoplasmic condition, particles are initialized uniformly in a 12 × 12 × 8 μm³ three-dimensional volume. Reflecting boundary conditions are applied at all domain walls. Time is discretized with a step of $\Delta t = 1$ s, and simulations are run for a total of 36,000 steps (10 hours), matching the duration of the opto-IRE1α live-cell imaging experiments.

Diffusion Model:

ER-tethered condition (2D with corrals). Membrane-bound IRE1α diffuses in the x-y plane with a size-dependent diffusion coefficient following the Saffman–Delbrück model for membrane proteins:

$$D_{mem}(n) = \frac{D_0}{n}$$

where $D_0 = 0.005$ μm²/s is the monomer diffusion coefficient on the ER membrane and n is the number of IRE1α molecules in the cluster. At each time step, each particle receives a Gaussian displacement in x and y:

$$\Delta x \sim N\left(0, \sqrt{2D_{mem}\Delta t}\right)$$

The ER membrane is modeled as a grid of square corrals with side length $L_1 = 1.2$ μm, representing the compartmentalization of the ER sheet by tubular structures. When a particle's proposed displacement would cross a corral boundary, the crossing is accepted with hopping probability p_{hol} and reflected otherwise. The base hopping probability is set to $p_{hol} = 3 \times 10^{-4}$, with a weak size-dependent correction:

$$p_{eff} = \min\left(1, p_{hop}\left(1 + 3\frac{r_{eff}}{L_c}\right)\right)$$

where $r_eff = r_0 \cdot n^{1/3}$ is the effective cluster radius (see below). This correction accounts for the fact that very large clusters may span multiple corrals and are therefore less affected by the confining geometry. The corral model produces subdiffusive motion ($\alpha < 1$) on timescales comparable to the corral exploration time $t^c \approx L^{c2} / (4D)$, because the mean squared displacement saturates once a particle has explored the interior of its corral.

Cytoplasmic condition (3D free Brownian motion). Cytoplasmic IRE1α diffuses freely in all three spatial dimensions. The diffusion coefficient follows the Stokes–Einstein relation for spherical clusters:

$$D_{cyto}(n) = \frac{D_0}{n^{1/3}}$$

where $D_0 = 0.15$ μm²/s for the cytoplasmic condition (30-fold higher than the membrane value, reflecting the lower viscous drag in the cytosol compared to a lipid bilayer). No corral boundaries are applied; the only spatial constraints are the reflecting domain walls. This produces normal Brownian diffusion with $\alpha \approx 1.0$ at all timescales.

Cluster Merging

At each time step, pairwise distances are computed between all clusters using SciPy's cdist function (2D Euclidean distance for ER, 3D for cytoplasm). Two clusters i and j merge irreversibly when their separation is less than the sum of their effective radii:

$$d(i,j) < r_{eff,i} + r_{eff,j}$$

where the effective radius of a cluster of n molecules is:

$$r_{eff} = r_0 \cdot n^{1/3}$$

with $r_0 = 0.05$ μm (50 nm), representing the interaction range of the CRY2olig photobody. The $n^{1/3}$ scaling assumes clusters are approximately spherical. Upon merging, the position of the surviving cluster is set to the mass-weighted center of the two original clusters, and the absorbed cluster is removed. Merging candidates are sorted by distance (closest first) to ensure deterministic behavior when multiple merging events are possible in a single time step.

Mean Squared Displacement Analysis

To extract the anomalous diffusion exponent α, we performed short tracking simulations that mimic the experimental MSD protocol. At selected analysis timepoints (1 hour and 4 hours), the current cluster configuration was extracted and subjected to 180 seconds of diffusion-only dynamics (no merging) recorded at 5-second intervals, matching the experimental imaging cadence. Three independent tracking replicates were performed per timepoint to improve statistics. For the ER condition, corral boundaries were preserved during tracking to capture the confining effect on the MSD. For the cytoplasmic condition, domain boundaries were removed (unwrapped coordinates) to prevent finite-box artifacts from introducing spurious subdiffusion.

The time-averaged MSD was computed for each cluster track:

$$MSD(\tau) = \left\langle \left(r(t+\tau) - r(t) \right)^2 \right\rangle$$

The anomalous diffusion exponent α was then obtained by fitting the power-law relationship:

$$MSD(\tau) = D_\alpha \cdot \tau^\alpha$$

Using ordinary least-squares regression on $\log_{10}(\text{MSD})$ versus $\log_{10}(\tau)$. Lags up to half the trajectory length were included. Values of $\alpha < 1$ indicate subdiffusive (confined) motion, $\alpha = 1$ indicates normal Brownian diffusion, and $\alpha > 1$ would indicate superdiffusion. Fitted α values were clipped to the range [0, 2] to exclude non-physical outliers arising from very short or noisy tracks.

Simulation Parameters

All simulation parameters are summarized in the table below.

Table 1:

Parameter	**Symbol**	**ER-tethered**	**Cytoplasmic**
Number of monomers	N	200	200
Domain (x × y)	$L_x \times L_\gamma$	12 × 12 μm²	12 × 12 μm²
Domain height	L_i	n/a (z = 0)	8 μm
Monomer diffusion coeff.	D_0	0.005 μm²/s	0.15 μm²/s
Time step	Δt	1 s	1 s
Total simulation time	T	36,000 s (10 h)	36,000 s (10 h)
Base merge radius	r_0	0.05 μm	0.05 μm
Corral side length	L^c	1.2 μm	n/a
Hopping probability	p_{hol}	3×10^{-4}	n/a
Snapshot interval		120 s (2 min)	120 s (2 min)
MSD tracking duration		180 s (3 min)	180 s (3 min)

Software and Reproducibility

The simulation was implemented in Python 3 using NumPy for vectorized Brownian dynamics, SciPy (scipy.spatial.distance.cdist) for pairwise distance computation during the merging step, and Matplotlib for figure generation and video rendering (via FFMpeg). All simulations used a fixed random seed (seed = 42) for reproducibility. The MSD tracking simulations used separate seeds (100–400 series) for each replicate. A single simulation (200 particles, 36,000 time steps) completes in ~5 seconds on a standard laptop. The complete simulation script (ire1_figure1_simulation.py) is available in the supplementary materials.

Resazurin Cell Viability Assay:

For cell viability assessments, cells were plated at approximately 10K cells/well in 96-well F-bottom plates (Greiner, #655090), with inner wells filled with 100 µL of DPBS to minimize evaporation. Cells were illuminated on day 1 according to their respective conditions, with light exposure intervals of 30 seconds over a 24-hour period. After 24 hours, a 10x solution of Resazurin (1 mM stock, final concentration 100 µM) was added to each well. The cells were incubated in the dark for 2 hours, and fluorescence measurements were obtained using a Cytation 5 (Biotek) plate reader (550 nm excitation, 590 nm emission). Each condition included five replicate wells, with five additional dark control wells per cell line.

Bulk RNA Sequencing (RNA-Seq):

HEK293T-cyto-opto-IRE1α and HEK293T-ER-opto-IRE1α cells were plated in 96-well F-bottom plates (Greiner, #655090) and allowed to adhere overnight. Cells were illuminated using the OptoPlate (Bugaj LJ and Lim WA, 2019) for a range of times (0-345 minutes, with lysates collected at 15-minute intervals). RNA was extracted using the RNeasy Kit (Qiagen, Cat: 74104). Library preparation and sequencing were outsourced to Novogene Bulk RNA-Seq Service (novogene.com). Paired-end FASTQ files were provided for each sample.

The FASTQ files were uploaded to the Galaxy server (The Galaxy Community, 2024) for further analysis. We used FastQC (version 0.12.1) to perform quality control and identify adapter sequences and low-quality reads. Reads were then trimmed with Trimmomatic (version 0.39) and aligned to the human reference genome (hg38) using RNA-STAR (version 2.7.11a). Gene counts and transcript lengths were calculated with featureCounts (version 2.0.8). TPM normalization was applied to the gene count and gene length data to standardize expression levels across different conditions.

Per IRE1α molecule normalization:

To normalize the RNA seq data to the protein expression levels of IRE1α, we performed a western blot of anti-Tot-IRE1α in ER and Cyto-opto-IRE1α cells (Fig. S2C). Then, we quantified band intensities and normalized to β-actin. To account for unequal IRE1α protein abundance between subcellular fractions, $\log_2$ fold change ($\log_2$FC) values were normalized prior to analysis. A normalization factor was calculated for each fraction by dividing the mean IRE1α signal intensity of that fraction by the overall mean IRE1α signal intensity across both fractions. The overall mean IRE1α intensity was calculated as the arithmetic mean of the ER and cytoplasmic fraction means: (3,144.48 + 16,468.07) / 2 = 9,806.28 arbitrary units. This yielded normalization factors of 0.321 for the ER fraction (3,144.48 / 9,806.28) and 1.679 for the cytoplasmic fraction (16,468.07 / 9,806.28). Normalized $\log_2$FC values for each fraction were then obtained by dividing the observed $\log_2$FC by the corresponding normalization factor

XBP1 Locus Sashimi Plot creation:

Aligned BAM files were loaded into the IGV genome viewer using the hg38 reference genome. We then focused on the XBP1 locus (ch22: 28794555-28800597) and generated a sashimi plot with six timepoints for both ER- and Cyto-opto-IRE1α. We only included junctions between exon 3 – exon 4, exon 4 – exon 5, and exon 3 – exon 5, as shown on the plot.

TCGA XBP1-es Analysis:

Three splice junctions were defined for PSI calculation: (1) the exon-skipping junction (XBP1-es; chr22:28,795,733–28,797,076), (2) the canonical exon 3–exon 4 junction (chr22:28,796,193–28,797,076), and (3) the canonical exon 4–exon 5 junction (chr22:28,795,733–28,796,046). All coordinates are in GRCh38 and represent intron boundaries (i.e., the last base of the upstream exon donor site to the first base of the downstream exon acceptor site).

Junction-level read counts were retrieved from the Snaptron RNA-seq junction database (v2; https://snaptron.cs.jhu.edu) using the exact-match query API (exact=1)[28]. The TCGA v2 compilation (recount3-based, hg38; 11,347 samples from The Cancer Genome Atlas) was queried. For each junction, per-sample read counts were extracted from the samples field of the Snaptron response.

Percent Spliced In (PSI) for the XBP1-es isoform was calculated using the standard cassette-exon formula consistent with rMATS convention:

$$PSI = \frac{C_{skip}}{C_{skip} + \frac{C_{E3\rightarrow E4} + C_{E4\rightarrow E5}}{2}}$$

where C_{skip} is the read count supporting the exon-skipping junction, and $C_{E3\rightarrow E4}$ and $C_{E4\rightarrow E5}$ are read counts supporting the two flanking canonical junctions. PSI was calculated only for samples with a denominator ≥ 5 reads to ensure reliable estimates, and is reported as a percentage (PSI × 100) throughout.

Western Blots:

In a 60-80% confluent plastic-bottom 6-well plate (Genesee, Cat: 25-105), cells were lysed using 150 uL per well of RIPA buffer (150mM NaCl, 1M Tris-HCl (pH 8.0), 1% Nonidet P40, 0.5% NaDC, 10% SDS). Lysates were briefly sonicated, centrifuged for 15 min at 14.5g, and stored at -80°C.

Lysates were thawed on ice, and then concentration was measured using the Bradford reagent kit protocol. Samples were diluted in 2x Laemmli buffer with 5% β-mercaptoethanol (BME) to ensure all samples had the same protein concentration. The samples were then boiled at 95°C for 5 minutes, briefly spun down, and stored at -20°C until SDS-PAGE was performed. Samples were run on 5%/10% two-layer SDS-PAGE gels at 105V for 1-2 hours, then transferred onto a PVDF membrane using Trans-Blot SD (Bio-Rad). PVDF membranes were cut where bands were expected, then blocked in 3% BSA diluted in TBS-T for 1 hour. The membranes were incubated overnight with primary antibodies diluted in 3% BSA-TBST. The next day, membranes were washed three times with TBS-T, each wash lasting 5 minutes. Afterward, the membranes were incubated with secondary antibodies for 1 hour, then washed three times with TBS-T. All membranes were imaged using the Li-Cor Odyssey instrument.

qRT-PCR:

Using 24-well plates at 60-80% confluence cells were illuminated using the OptoPlate plate. Right after illumination lysis and RNA purification was done according to the RNeasy kit (Qiagen: Cat#74104) protocol. Reverse Transcription was performed using the Qiagen RT kit

(Qiagen). We then quantified cDNA concentration using the Qubit 4 Fluorometer using the ssDNA kit. We then diluted all samples down to 10ng/uL cDNA concentration for use in PCR. PCR was performed using the SYBR Green Master Mix (Cat: 4364344) and run in triplicate on the Bio-Rad CFX96 Touch System. Ct values were analyzed using the Double Delta Ct analysis [36]. For RT-PCR of the XBP1 amplicon, we used previously validated primers[21] and ran the samples on a 4% gel for 30 minutes. Each PCR reaction contained approximately 60 ng of cDNA and was performed using Primestar GXL (R051A) under standard conditions.

For PAIR2 and Actinomycin D experiments, compounds were added to cells ~30 min prior to illumination. PAIR2 concentration varied depending on experiment, while Actinomycin D was used only at a concentration of 1 ug/mL.

References:

1. Wood, C. D., Thornton, T. M., Sabio, G., Davis, R. A. & Rincon, M. Nuclear Localization of p38 MAPK in Response to DNA Damage. *Int. J. Biol. Sci.* **5**, 428–437 (2009).
2. Snead, W. T. *et al.* Membrane surfaces regulate assembly of ribonucleoprotein condensates. *Nat. Cell Biol.* **24**, 461–470 (2022).
3. Santos, S. D. M., Verveer, P. J. & Bastiaens, P. I. H. Growth factor-induced MAPK network topology shapes Erk response determining PC-12 cell fate. *Nat. Cell Biol.* **9**, 324–330 (2007).
4. Moriizumi, H. *et al.* Spatiotemporal regulation of MKK4 dictates switch-like JNK activation and binary cell-fate decisions. *Nat. Commun.* **17**, 97 (2026).
5. Newton, A. C., Bootman, M. D. & Scott, J. D. Second Messengers. *Cold Spring Harb. Perspect. Biol.* **8**, a005926 (2016).
6. Baudet, S. *et al.* Subcellular second messenger networks drive distinct repellent-induced axon behaviors. *Nat. Commun.* **14**, 3809 (2023).

7. Siwecka, N. *et al.* The Structure, Activation and Signaling of IRE1 and Its Role in Determining Cell Fate. *Biomedicines* **9**, 156 (2021).
8. Scheper, W. & Hoozemans, J. J. M. The unfolded protein response in neurodegenerative diseases: a neuropathological perspective. *Acta Neuropathol. (Berl.)* **130**, 315–331 (2015).
9. McGrath, E. P. *et al.* The Unfolded Protein Response in Breast Cancer. *Cancers* **10**, (2018).
10. Smith, J. W., Wilburn, D. B. & Belyy, V. Direct optical activation of human IRE1 identifies unique patterns of transcriptional and post-transcriptional mRNA regulation in the unfolded protein response. *J. Biol. Chem.* **302**, 111067 (2026).
11. Han, D. *et al.* IRE1α Kinase Activation Modes Control Alternate Endoribonuclease Outputs to Determine Divergent Cell Fates. *Cell* **138**, 562–575 (2009).
12. Hollien, J. & Weissman, J. S. Decay of Endoplasmic Reticulum-Localized mRNAs During the Unfolded Protein Response. *Science* **313**, 104–107 (2006).
13. Belyy, V., Zuazo-Gaztelu, I., Alamban, A., Ashkenazi, A. & Walter, P. Endoplasmic reticulum stress activates human IRE1α through reversible assembly of inactive dimers into small oligomers. *eLife* **11**, e74342 (2022).
14. Gómez-Puerta, S. *et al.* Live imaging of the co-translational recruitment of XBP1 mRNA to the ER and its processing by diffuse, non-polarized IRE1α. *eLife* **11**, e75580 (2022).
15. Shemorry, A. *et al.* Caspase-mediated cleavage of IRE1 controls apoptotic cell commitment during endoplasmic reticulum stress. *eLife* **8**, e47084 (2019).
16. Hernández-Díaz, T. *et al.* Activation of IRE1 Endonuclease Activity Regulates Zika Virus Replication and Antiviral Response During Infection in Human Microglia. *Viruses* **17**, 1291 (2025).

17. Niwa, M., Sidrauski, C., Kaufman, R. J. & Walter, P. A Role for Presenilin-1 in Nuclear Accumulation of Ire1 Fragments and Induction of the Mammalian Unfolded Protein Response. *Cell* **99**, 691–702 (1999).
18. Jaskulska, A., Janecka, A. E. & Gach-Janczak, K. Thapsigargin—From Traditional Medicine to Anticancer Drug. *Int. J. Mol. Sci.* **22**, (2020).
19. Orsi, A. *et al.* Congress of multiple dimers is needed for cross-phosphorylation of IRE1α and its RNase activity. *Life Sci. Alliance* **7**, e202302562 (2024).
20. Taslimi, A. *et al.* An optimized optogenetic clustering tool for probing protein interaction and function. *Nat. Commun.* **5**, 4925 (2014).
21. Feldman, H. C. *et al.* ATP-Competitive Partial Antagonists of IRE1α's RNase Segregate Outputs of the UPR. *Nat. Chem. Biol.* **17**, 1148–1156 (2021).
22. Belyy, V., Tran, N.-H. & Walter, P. Quantitative microscopy reveals dynamics and fate of clustered IRE1α. *Proc. Natl. Acad. Sci.* **117**, 1533–1542 (2020).
23. Ong, G. *et al.* IRE1 signaling increases PERK expression during chronic ER stress. *Cell Death Dis.* **15**, 276 (2024).
24. Bugaj, L. J. & Lim, W. A. High-throughput multicolor optogenetics in microwell plates. *Nat. Protoc.* **14**, 2205–2228 (2019).
25. Bright, M. D., Itzhak, D. N., Wardell, C. P., Morgan, G. J. & Davies, F. E. Cleavage of BLOC1S1 mRNA by IRE1 Is Sequence Specific, Temporally Separate from XBP1 Splicing, and Dispensable for Cell Viability under Acute Endoplasmic Reticulum Stress. *Mol. Cell. Biol.* **35**, 2186–2202 (2015).
26. Ghosh, R. *et al.* Allosteric Inhibition of the IRE1α RNase Preserves Cell Viability and Function during Endoplasmic Reticulum Stress. *Cell* **158**, 534–548 (2014).

27. Duarte, M. *et al.* Rotavirus Infection Alters Splicing of the Stress-Related Transcription Factor XBP1. *J. Virol.* **93**, 10.1128/jvi.01739-18 (2019).
28. Wilks, C., Gaddipati, P., Nellore, A. & Langmead, B. Snaptron: querying splicing patterns across tens of thousands of RNA-seq samples. *Bioinformatics* **34**, 114–116 (2018).
29. Wiese, W. *et al.* Endoplasmic Reticulum Stress in Acute Myeloid Leukemia: Pathogenesis, Prognostic Implications, and Therapeutic Strategies. *Int. J. Mol. Sci.* **26**, (2025).
30. Oliver, L. *et al.* Assessment of caspase activity as a possible prognostic factor in acute myeloid leukaemia. *Br. J. Haematol.* **118**, 434–437 (2002).
31. Krawiec, K. *et al.* Targeting Apoptosis in AML: Where Do We Stand? *Cancers* **14**, (2022).
32. Lemaitre, F. *et al.* The transcription factor c-Jun inhibits RBM39 to reprogram pre-mRNA splicing during genotoxic stress. *Nucleic Acids Res.* **50**, 12768–12789 (2022).
33. Jiang, D., Niwa, M. & Koong, A. C. Targeting the IRE1α–XBP1 branch of the unfolded protein response in human diseases. *Semin. Cancer Biol.* **33**, 48–56 (2015).
34. Philippe, C. *et al.* Pivotal role of the endoplasmic reticulum stress-related XBP1s/miR-22/SIRT1 axis in acute myeloid leukemia apoptosis and response to chemotherapy. *Leukemia* **38**, 1764–1776 (2024).
35. Zhong, Y. *et al.* A novel XBP1 variant is highly enriched in cancer tissues and is specifically required for cancer cell survival. *Biochem. Biophys. Res. Commun.* **562**, 69–75 (2021).
36. Livak, K. J. & Schmittgen, T. D. Analysis of Relative Gene Expression Data Using Real-Time Quantitative PCR and the 2−ΔΔCT Method. *Methods* **25**, 402–408 (2001).

Supplementary Files

This is a list of supplementary files associated with this preprint. Click to download.

- SupplementaryVideo6.mp4
- SupplementaryVideo3.mp4
- SupplementaryVideo1.mp4
- SupplementaryVideo8.mp4
- SupplamentalFiguresFinal.pdf
- SupplementaryVideo4.mp4
- SupplementaryVideo7.mp4
- SupplementaryVideo2.mp4
- SupplementaryVideo5.mp4
- SupplementaryDataIRE1paper.xlsx